



# LUND UNIVERSITY

## Development and characterization of a multiple-coincidence ion-momentum imaging spectrometer.

Laksman, Joakim; Céolin, Denis; Månsson, Erik; Ristinmaa Sörensen, Stacey; Gisselbrecht, Mathieu

*Published in:*  
Review of Scientific Instruments

*DOI:*  
[10.1063/1.4853435](https://doi.org/10.1063/1.4853435)

2013

[Link to publication](#)

### *Citation for published version (APA):*

Laksman, J., Céolin, D., Månsson, E., Ristinmaa Sörensen, S., & Gisselbrecht, M. (2013). Development and characterization of a multiple-coincidence ion-momentum imaging spectrometer. *Review of Scientific Instruments*, 84(12), Article 123113. <https://doi.org/10.1063/1.4853435>

*Total number of authors:*  
5

### **General rights**

Unless other specific re-use rights are stated the following general rights apply:  
Copyright and moral rights for the publications made accessible in the public portal are retained by the authors and/or other copyright owners and it is a condition of accessing publications that users recognise and abide by the legal requirements associated with these rights.

- Users may download and print one copy of any publication from the public portal for the purpose of private study or research.
- You may not further distribute the material or use it for any profit-making activity or commercial gain
- You may freely distribute the URL identifying the publication in the public portal

Read more about Creative commons licenses: <https://creativecommons.org/licenses/>

### **Take down policy**

If you believe that this document breaches copyright please contact us providing details, and we will remove access to the work immediately and investigate your claim.

LUND UNIVERSITY

PO Box 117  
221 00 Lund  
+46 46-222 00 00

## Development and characterization of a multiple-coincidence ion-momentum imaging spectrometer

J. Laksman, D. Céolin, E. P. Månsson, S. L. Sorensen, and M. Gisselbrecht

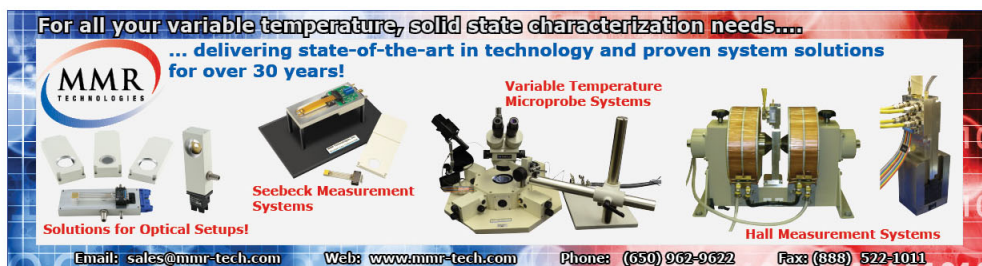
Citation: [Review of Scientific Instruments](#) **84**, 123113 (2013); doi: 10.1063/1.4853435

View online: <http://dx.doi.org/10.1063/1.4853435>

View Table of Contents: <http://scitation.aip.org/content/aip/journal/rsi/84/12?ver=pdfcov>

Published by the [AIP Publishing](#)

---



For all your variable temperature, solid state characterization needs....  
... delivering state-of-the-art in technology and proven system solutions  
for over 30 years!

**MMR TECHNOLOGIES**

**Seebeck Measurement Systems**

**Variable Temperature Microprobe Systems**

**Hall Measurement Systems**

Solutions for Optical Setups!

Email: [sales@mmr-tech.com](mailto:sales@mmr-tech.com) Web: [www.mmr-tech.com](http://www.mmr-tech.com) Phone: (650) 962-9622 Fax: (888) 522-1011

# Development and characterization of a multiple-coincidence ion-momentum imaging spectrometer

J. Laksman,<sup>a)</sup> D. Céolin,<sup>b)</sup> E. P. Månsson, S. L. Sorensen,<sup>c)</sup> and M. Gisselbrecht  
*Department of Synchrotron Radiation Research, Lund University, Box 118, S-221 00 Lund, Sweden*

(Received 12 November 2013; accepted 8 December 2013; published online 27 December 2013)

The design and performance of a high-resolution momentum-imaging spectrometer for ions which is optimized for experiments using synchrotron radiation is presented. High collection efficiency is achieved by a focusing electrostatic lens; a long drift tube improves mass resolution and a position-sensitive detector enables measurement of the transverse momentum of ions. The optimisation of the lens for particle momentum measurement at the highest resolution is described. We discuss the overall performance of the spectrometer and present examples demonstrating the momentum resolution for both kinetics and for angular measurements in molecular fragmentation for carbon monoxide and fullerenes. Examples are presented that confirm that complete space-time focussing is possible for a two-field three-dimensional imaging spectrometer. © 2013 Author(s). All article content, except where otherwise noted, is licensed under a Creative Commons Attribution 3.0 Unported License. [<http://dx.doi.org/10.1063/1.4853435>]

## I. INTRODUCTION

Fundamental questions regarding photo induced chemical reactions, transient states in molecules, and dissociative states are of central importance to chemical physics. New scientific tools based upon spectroscopic imaging and multi coincidence experiments have emerged to address some of these issues, and have achieved great success in dynamic studies of ionised molecules and clusters using lasers, synchrotron radiation, and in collision experiments.<sup>1-5</sup>

Synchrotron radiation is a unique light source providing the ability to selectively ionize particular electronic shells, excite localized core-electronic states, and to select the polarisation of the light. In this context, spectroscopic imaging instruments of various designs<sup>6-10</sup> allow recording the velocity or momenta of several reaction products in coincidence with energy-analyzed electrons to reveal the details of dissociative states in molecules.

Velocity imaging methods take advantage of efficient two-dimensional position-sensitive detectors to measure molecular photodissociation products.<sup>12,13</sup> Implementation of a focusing lens to improve velocity resolution extended the imaging method significantly<sup>14</sup> and several implementations of velocity imaging for synchrotron applications have been developed.<sup>8,11</sup> While 2D imaging is advantageous for low repetition-rate measurements, three-dimensional imaging techniques using timing detectors do not require the Abel inversion and can be used for multi-coincidence measurements without constraints on the polarisation of the light.<sup>15</sup> The space-time focussing condition is widely utilised in linear time-of-flight spectrometers, known as the Wiley-McLaren condition,<sup>16</sup> but so far a general solution for three-

dimensional velocity-focusing spectrometers has been elusive and several groups concluded that it was impossible to meet the required conditions with 1-field<sup>7</sup> and 2-field<sup>6</sup> Wiley-McLaren spectrometer. The aim of the present study is to address the issue of fully three-dimensional velocity-focusing and to present a spectrometer design compatible with it in order to study molecules and clusters.

We constructed a 2-field ion momentum-imaging spectrometer with high mass resolution,  $4\pi$  collection efficiency for ion energies up to 15 eV, and high velocity resolution even with an extended ion source. The geometry and fields of the spectrometer are adapted to achieve fully three-dimensional focusing, where an electrostatic lens reduces the effect of the source volume. In this paper we describe the design and performance of the instrument; we derive a semi-analytical expression from the space-time to momentum inversion, and present examples that illustrate how high kinetic-energy resolution illuminates details in the final dissociative states for carbon monoxide. The isotope-resolved fullerene mass spectrum exemplifies the high mass resolution of the spectrometer.

## II. DESIGN OF THE SPECTROMETER AND SETUP

The spectrometer is designed primarily for use with linearly polarized synchrotron radiation in the soft x-ray region. The polarization and propagation direction of the light lie in the xy-plane and the spectrometer axis (z) is vertical. The detector is in the x-y plane. The background pressure is about  $10^{-8}$  mbar. The sample can be either an effusive jet of gas or a molecular beam which crosses the photon beam in the horizontal plane. A molecular beam is used for fullerene experiments presented in Sec. III where a beam of fullerene molecules was produced by evaporation of a commercially obtained powder sample (99.95% purity) in an oven at 600 °C in front of a 1 mm skimmer to limit the divergence of the molecular beam. The translational energy transverse to the

<sup>a)</sup>Present address: MAX IV Laboratory, Lund University, Box 118, S-221 00 Lund, Sweden.

<sup>b)</sup>Also at Synchrotron SOLEIL, L'Orme des Merisiers, St. Aubin BP 48, F-91192 Gif-Sur-Yvette, France.

<sup>c)</sup>Electronic mail: stacey.sorensen@sljus.lu.se



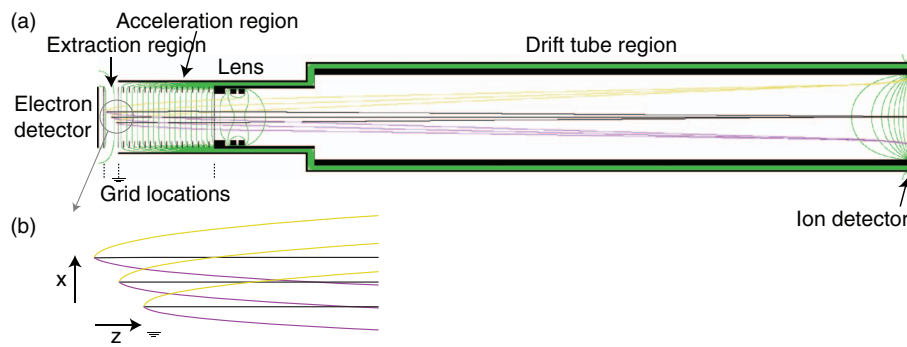


FIG. 1. (a) Schematic drawing of the spectrometer. The grid on the right side of the extraction region is grounded. The electric field contours are shown in green. (b) Trajectories for three initial velocity directions are drawn from three different source points (spaced by  $\pm 5$  mm in  $x$  and  $z$ ) to illustrate the radial focusing, for ions with a kinetic energy of 10 eV. Regardless of source point, the  $v_x$  component determines the position on the detector in (a).

molecular beam, i.e., along the spectrometer axis was thus reduced.

## A. Spectrometer

The performance of our spectrometer was investigated simulating particle trajectories with SIMION.<sup>17</sup> Trajectories for 10 eV ions are illustrated in Fig. 1(a). Electrons and ions are detected by micro channel plates, (MCP), on the ion side (right) followed by a position-sensitive delay-line anode of 80 mm diameter (Roentdek DLD-80). The 40 mm electron detector (left) is located near the source region to provide the start signal for the ion flight time measurement. Time differences between the amplified start and delay-line signals give three coordinates (time and position) which are transformed to obtain the initial momentum vectors of positive ions. The delay-line anode has spatial resolution of better than 0.1 mm, and the overall temporal resolution of the system is about 1 ns.

The extraction region has grids for electrons and ions both located 7 mm from the source point. It is followed to the right in Fig. 1(a) by a region with an accelerating, uniform field created by a series of electrodes. The total length of the spectrometer including the 94 mm long acceleration region and the drift tube is about 750 mm. Metal grids are used to maintain a high degree of field uniformity where the field gradient is high but since the transmission efficiency of the grids is about 80% these are used sparingly. The spectrometer is enclosed in an electrically grounded aluminum cylinder for shielding but no magnetic field shielding is used.

In all coincidence experiments the aim is to detect particles which originate in the same photoionization event. False coincidences may be detected if another ionization event occurs within the time window used for the flight-time,  $t_{\max}$ . If we define the variable  $x = \lambda t_{\max}$  then the optimal ionization rate  $\lambda$  can be determined from the Poisson probability  $f_x(k)$  for  $k$  ionization events to occur:

$$f_x(k) = \frac{x^k e^{-x}}{k!}. \quad (1)$$

For a measurement with 99% true coincidences (represented by  $k = 0$ ) and a measurement interval of  $t_{\max} = 10 \mu\text{s}$  the event count rate should be less than  $10^3$  Hz.

The detection efficiency of the spectrometer system for a single particle is the product of the geometrical factor derived from the open-area ratio of grids (80%) and the efficiency of the detector. The detector efficiency must be calibrated in order to obtain accurate values, but typically 40% of ions and 60% of electrons that reach the detector are registered. For photon energies well above the double-ionization threshold several electrons are produced. Assuming that the detection of each electron is independent, the probability to get a start signal increases to  $1 - (1 - 0.8 \cdot 0.6)^n$ , e.g., 86% in the case of triple ionization ( $n = 3$ ). When three ions are produced, the probability for all particles to be detected after an electron start signal is  $(0.8^2 \times 0.4)^3 \approx 2\%$  (ions pass through two grids). Two out of three ions can be detected with a probability of 15%, while one of them is detected with 43% probability. This leads to a relatively high incidence of “aborted ion coincidences” in multi-fragmentation of molecules which must be taken into account if accurate branching ratios are needed.

## B. Mass resolution

The basic principle of the time-of-flight spectrometer is to disperse particles in time according to their mass by acceleration in a uniform electric field. The time  $T_0$  for an ion with initially zero kinetic energy to travel through the entire spectrometer was derived by Wiley and McLaren<sup>16</sup> by separating the spectrometer into three regions, the extraction region (length  $s$ ), the acceleration region of length  $d$ , and the field-free drift tube with length  $D$ . The total flight time for a particle of mass  $m$  and charge  $q$  is then

$$T_0 = T_{\text{ext}} + T_A + T_D = \alpha \sqrt{m/q}, \quad (2)$$

where  $\alpha$  contains all the spectrometer parameters and the time scale for  $T_0$  has been calibrated by subtracting a constant dependent on the experimental set-up.

If the source has ions with kinetic energy  $E_k$  the resulting temporal spread is expressed as

$$\Delta T_k = \frac{\sqrt{2 \cdot m \cdot E_k}}{q \cdot E_{\text{ext}}}, \quad (3)$$

where  $E_{\text{ext}}$  and  $E_A$  are the fields applied in the extraction and acceleration regions. Seccombe *et al.*<sup>18</sup> showed that the time interval between two ions is  $T_{m+1} - T_m \approx \alpha / (2\sqrt{mq}) \cdot 1 \text{ u}$ .

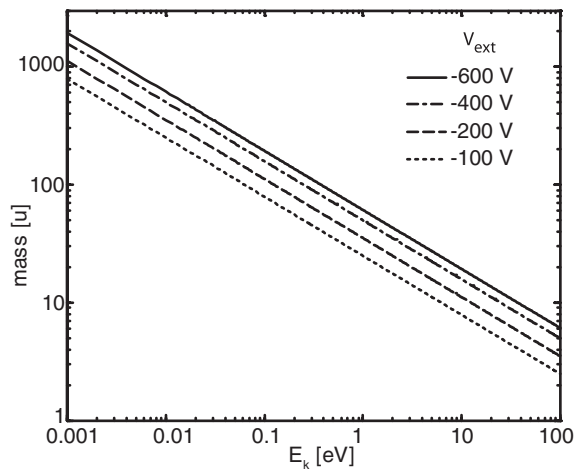


FIG. 2. The largest resolvable mass calculated as a function of ion kinetic energy,  $E_k$ . The largest resolvable mass (for  $q = 1 e$ ) is shown for different extraction voltages ( $V_{\text{ext}}$ ) under the Wiley-McLaren focusing condition.

If the temporal separation between ions is greater than twice the line broadening in Eq. (3) then the ion peaks can be resolved. This kinetic-energy constraint limits the resolution of the instrument to masses fulfilling the condition:

$$m < \frac{\alpha \cdot E_{\text{ext}}}{\sqrt{32 \cdot E_k/q}}. \quad (4)$$

Equation (4) expresses the maximum resolving power as a function of the applied voltages, ion kinetic energy, and charge. The maximum  $m$  is calculated analytically as a function of kinetic energy for different extraction voltages is plotted on a log/log scale for  $q = 1$  in Fig. 2. The graph shows that ions of mass  $\sim 10$  u can be resolved if the kinetic energy does not exceed  $\sim 10$  eV. Clusters with masses of  $\sim 1000$  u can be resolved up to few meV, an energy comparable to typical thermal energies.

### C. Axial and transverse focusing of ions

We have explored the design of a 2-field Wiley-McLaren spectrometer with the goal to combine spatial-temporal focusing to achieve high mass resolution and velocity focusing to compensate for the reduction in momentum resolution arising from an extended source volume in the  $xy$ -plane. The simulated trajectories for up to  $E_k = 10$  eV in directions parallel, antiparallel, and perpendicular to the spectrometer axis indicated that the optimal conditions are reached when the following relations between the ion extraction potential ( $V_{\text{ext}}$  at the grid on the electron-side), the applied drift-tube potential ( $V_D$ ), and the lens potential ( $V_L$ ) are fulfilled:

$$V_{\text{ext}} \approx -0.1 \cdot V_D \quad \text{and} \quad V_L \approx 0.8 \cdot V_D. \quad (5)$$

Here the middle grid in Fig. 1(a) produces a field of  $E_{\text{ext}} (= V_{\text{ext}}/2s)$  of  $\sim 200$  V/cm. The lens potential for optimal focusing at this value is obtained from the simulation. Eliminating the grid in front of the ion detector improves the spectrometer transmission but also introduces a field inhomogeneity that defocuses the ions. We find that with the MCP at

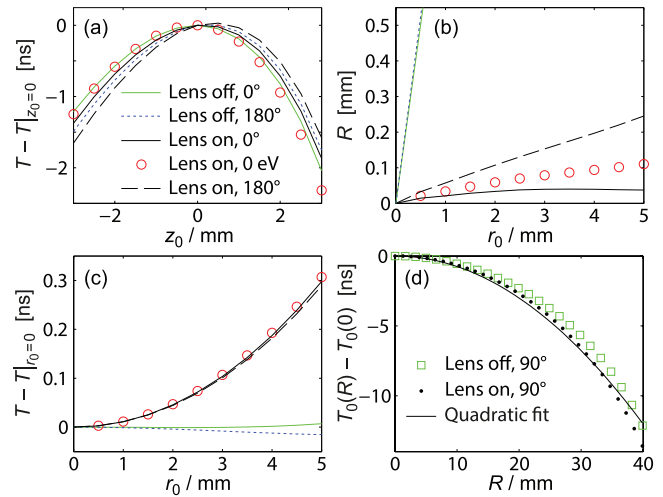


FIG. 3. Simulated performance for 3D-focusing of 10 u ions with 10 eV energy and for different elevation angles with respect to the  $z$ -axis. Ions with zero kinetic energy are also included for comparison (rings). (a) The deviation from the nominal time of flight for ions originating at different longitudinal positions. The time deviation is by definition zero for the nominal source point at  $z_0 = 0$ . The simulation compares two lens potentials (on and off). Wiley-McLaren time-focusing to the first order is achieved in both cases. (b) The detection radius,  $R$ , is shown as a function of radial source position for the same five cases, all without transverse momentum. Enabling the radial lens reduces the spread caused by the extended source to less than 1/20. (c) The deviation from nominal time of flight for ions originating at different radii is affected by the lens, but this is a minor effect compared to (a). (d) The coupling between initial transverse momentum (proportional to  $R$  on the detector) and the flight time is determined by all field inhomogeneities. This deviation may exceed 10 ns at large radii, while the contribution by the focusing lens is much smaller. The total deviation can be accounted for by a quadratic correction (Eq. (8)).

the drift tube potential we achieve the same performance level via minor adjustments to the lens settings ( $V_L$  and  $V_{\text{ext}}$ ).

Simulated trajectories for these settings are shown in Fig. 1, while the lens performance is investigated in greater detail in Fig. 3. Simulations were done without kinetic energy (rings) and with 10 eV directed along (solid line,  $0^\circ$  elevation angle) or opposite (dashed line,  $180^\circ$ ) the spectrometer  $z$ -axis. The case without radial lens is also included (blue and green). For each curve the time of flight from the nominal source point  $r_0 = z_0 = 0$  defines the zero of the time axis.

The extent of the source along the  $z$  axis gives a temporal spread that can be minimised by appropriate focusing potentials. Figure 3(a) shows the time-focusing as a stationary point with the first derivative  $dT/dz_0 = 0$  for two ion emission angles. For  $|z_0| < 2$  mm the higher derivatives give less than 1 ns deviation, with a very small dependence on ion energy and the radial lens. In practice the range of  $z_0$  is determined by the dimensions of the source volume (the intersection between the sample and the photon beam). Typical values are less than 1 mm, thus the temporal extension is negligible.

The radial focusing of the source volume is investigated in Fig. 3(b). Without the radial lens, detector impact occurs at the same radius as the source point,  $R \approx r_0$ . With the electrostatic lens enabling the resulting inhomogeneous field (see Fig. 1) guides ions with identical momenta to a  $R < 0.5$  mm sized spot on the detector even when they originate at very different positions. The lens improves the average resolution

to  $R \approx r_0/40$  in the simulation. The same level of improvement is achieved in  $\Delta R$  for transverse momenta. The fact that ions from  $r_0 = 5$  mm impact at a slightly larger detector radius if their initial direction was in the backward direction than the forward direction (i.e., spending more time in the source region) indicates a slight field penetration in the source region. However, it remains near the limit of the 0.1 mm grid size used in the simulation. In Fig. 3(c) the temporal deviation caused by the lens is shown to be less than 0.3 ns for points within a 5 mm source up to 10 eV kinetic energy. All times in Fig. 3 can be rescaled to another ion mass via their proportionality to  $\sqrt{m/q}$ .

We conclude from Figs. 3(a)–3(c) that the homogenous and inhomogenous fields together effectively focus in all three dimensions of velocity space. The potentials used in the simulated trajectories shown in Fig. 1 achieve proper three-dimensional velocity-focusing for 10 eV kinetic-energy ions. The most significant conclusion we can draw is that the radial lens has no detrimental impact on the Wiley-McLaren focusing condition, confirming that this approach to separating spatial and temporal focusing is tractable.

#### D. Data treatment and examples

The first step in the data treatment is the transformation of raw time and position data into linear momentum. To take into account the electrostatic lenses, we employ a semi-analytical approach that starts by decoupling the axial and transverse motions and inserting coupling as a perturbation. This approach is supported by numerical simulations, and can be thought of as a paraxial approximation. Cylindrical coordinates are used in this section.

If we initially assume that all fields are homogeneous, i.e., no radial lens is used, then the transverse momentum is simply  $p_R = mR/T$ , where  $R$  is the radial position on the detector. The general first-order expression for the transformation of the TOF into initial axial momentum  $p_z$  is

$$p_z = q \cdot E_{\text{ext}} \cdot \Delta T, \quad \Delta T = T - T_0(R). \quad (6)$$

In the homogeneous-field case there is no  $R$ -dependence and  $T_0$  is the nominal flight time given by Eq. (2).

A radial lens introduces field inhomogeneities that must be taken into account in the transformations. Simulations following Eq. (5) for  $p_z = 0$  and the full range of detectable radial momenta showed that the transverse momentum can be described accurately by a radial magnification factor  $\mathcal{M}_R$ :

$$p_R = \frac{m \cdot R}{T \cdot \mathcal{M}_R}. \quad (7)$$

Inhomogenous fields also introduce a coupling between the transverse momentum and the flight time. We evaluate how the time  $T_0(R)$  for  $p_z = 0$  depends upon  $p_R$  in Fig. 3(d). The difference between the curves with and without the lens potentials is very small, thus the main origin of the temporal deviation for ions arriving at larger radii is the inhomogeneous field at the end of the drift tube. Regardless of origin, the deviation can be approximated by an  $R^2 T_0(0)$  term (solid line in

Fig. 3(d)). We can thus complete Eq. (6) with the definition

$$T_0(R) = [1 + c_2 R^2] \cdot \underbrace{\alpha \sqrt{m/q}}_{T_0(0)}, \quad (8)$$

where the proportionality constant  $c_2$  is determined by a fit to the simulation to be  $c_2 = -2.45 \text{ m}^{-2}$ . The same  $R^2$ -dependence was found by Lebech *et al.*<sup>7</sup> with a compact 1-field spectrometer, although their central time of flight was defined differently. Including an  $R^4$ -term makes the simulated curve indistinguishable from the points in Fig. 3(d) for coefficients  $c_2 = -2.0 \text{ m}^{-2}$ ,  $c_4 = -459 \text{ m}^{-4}$ .

Empirically, Eq. (8) holds also for  $p_z \neq 0$ , which confirms the validity of the paraxial approximation. For realistic ion energies, the substantial axial velocity induced by the electric fields in the extraction and acceleration regions of our spectrometer is high enough to make trajectory angles small at the entrance of the electrostatic lens, regardless of the initial direction. This allows us to neglect lens aberrations and nonlinearities in the axial motion, and is likely the reason that the nominal flight time is only increased by about 2%.

For each ion, the coordinates  $(\theta, p_R, p_z)$  in cylindrical momentum space can now be obtained from the recorded impact times and positions. The total kinetic energy is  $E_k = (p_R^2 + p_z^2)/(2m)$ .

### III. EXAMPLES OF THE PERFORMANCE OF THE SPECTROMETER

Multicoincident measurement of the fully three-dimensional fragment momenta from the dissociation of doubly charged carbon monoxide is an illuminating example to illustrate the performance of the spectrometer. Resonant excitation of carbon monoxide C 1s electrons leads to the emission of fragments with a well-defined angular anisotropy, and the dissociation channels are well studied in independent measurements. The coincident detection of fragments allows an unambiguous assignment of ions to dication dissociation. Figure 4 shows the time-of-flight-radius correlation plot for  $\text{C}^+$  ions measured in coincidence with  $\text{O}^+$  from carbon monoxide excited to the  $\text{C } 1s^{-1}\pi^*$  state at 287.40 eV. Each dashed curve corresponds to a fixed elevation angle of the momentum vector with respect to the spectrometer axis (the curve for  $90^\circ$  emission angle represents Eq. (8)). Each solid curve corresponds to a fixed kinetic energy; the innermost is 0.1 eV and the maximum detectable kinetic energy for these voltage settings is the outermost 12 eV. The overall agreement between the measured distribution and the calculated curves is very good.

#### A. Fragmentation of the carbon monoxide dication

The kinetic energy released in photo fragmentation can be determined by accurate measurement of the ion momenta, and the total fragment energy can be correlated to dication states in molecules via the total kinetic energy imparted to the fragments in a two-body dissociation process. This example demonstrates that detailed information on the fragmentation dynamics of CO molecules after resonant

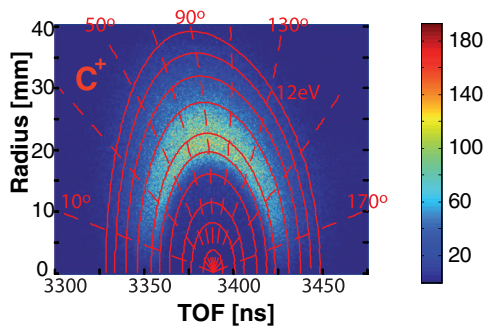


FIG. 4. The ion momentum represented in a time vs. radius correlation plot of the fragment  $C^+$  from the  $C^+/O^+$  fragment pair after excitation to the  $C\ 1s^{-1}\pi^*$  state in CO at 287.40 eV. The ion kinetic energy scale is indicated in the plot.

excitation can be obtained with our spectrometer. Linear momentum is conserved for all two-body fragmentation processes in the rest frame of the molecule. This is expressed as  $\frac{E_{O^+}}{m_{O^+}} - \frac{E_{C^+}}{m_{C^+}} = \Delta/m$  with  $m = \sqrt{m_{O^+}m_{C^+}}$  as the geometric mean mass, where  $\Delta$  represents the measured width of the correlation. Figure 5(a) shows the kinetic-energy correlation for  $O^+$  and  $C^+$  from  $CO^{2+}$ . Each spot along the diagonal  $\frac{E_{C^+}}{m_{C^+}} + \frac{E_{O^+}}{m_{O^+}} = v/m$  corresponds to fragmentation from a distinct dissociative state in the dication (see Fig. 5(c)). The width of the distribution perpendicular to this line,  $\Delta$ , reflects the overall energy resolution of the spectrometer, including thermal broadening in the source (here an effusive gas jet).

We find the energy broadening,  $\Delta$ , for the present case to be  $\sim 1.8$  eV. In Fig. 5(c) the distribution of total kinetic energy is plotted for the ion pairs shown in subplot (a). The states involved in fragmentation can be identified by comparing the peak energies to the difference between known dication state energies and atomic ion energies. If we assume that all frag-

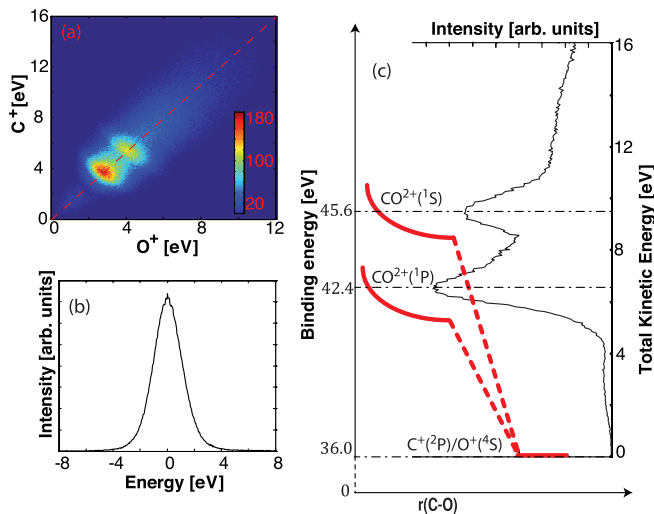


FIG. 5. (a) The kinetic-energy correlation between  $C^+$  and  $O^+$  ions measured after  $C\ 1s-\sigma^*$  excitation in carbon monoxide. (b) The integration of the distribution along the diagonal. The primary contribution to the width arises from the resolution of the spectrometer and the thermal energy of the molecules. (c) The total kinetic energy distribution is shown with a black line; this is a histogram of the sum of the two fragment energies. The peaks visible in the plot correspond to dissociation from the dication potential energy surfaces to the left to the fragment ground states (bottom).

ments are produced in the ground state [ $C^+(^2P)$  and  $O^+(^4S)$ ] then zero kinetic-energy release corresponds to an energy 36 eV above the neutral CO ground state; that scale is shown above (c). The most intense peak at 6.5 eV kinetic energy is attributed to fragmentation from the  $CO^{2+}(^1\Pi)$  electronic state located in the 41.8–43 eV binding-energy region. Peaks are also seen for the  $^3\Sigma$  state at  $\sim 43.5$  eV and  $^1\Sigma$  state at 45.3 eV (the latter is sharp when exciting the  $C\ 1s \rightarrow \sigma^*$  resonance instead, not shown). The broad shoulder at  $\sim 3.5$  eV kinetic energy is interpreted as a sequential process where Auger decay populates repulsive states in  $CO^{+*}$  in the binding energy region 36–41 eV that dissociate into  $C^+(^2P) + O^*$  which autoionizes to  $O^*(^3D, ^3F, ^3P)$  at 36.5 eV. All energies are thus in excellent agreement with published results.<sup>19,20</sup> While this measurement cannot be considered to be a fixed-in-space molecule measurement the angular distribution of the emitted fragments does reflect the molecular geometry, and for a resonant excitation we expect alignment to occur by selective excitation. Both the direction of the transition dipole moment and the molecular geometry will influence the angular anisotropy within the dipole approximation.

The images shown in Figs. 6(a) and 6(b) show the distribution of fragments in the plane of the detector. These correspond exactly to velocity map images.<sup>14</sup> The alignment of the carbon monoxide molecule is indicated to the right with the thin arrow indicating the direction of the polarization vector. The alignment of the molecule is seen in the fragment distribution: the  $C\ 1s^{-1}\pi$  resonance implies alignment of the molecular bond perpendicular to the polarisation vector and for the  $C\ 1s^{-1}\sigma^*$  resonance the alignment is parallel.

The three-dimensional distribution of ejected fragments shown in Fig. 6(c) motivates a coordinate transformation to a spherical coordinate system,  $(\theta, \phi, p)$ , where the angles refer to the orientation before fragmentation and  $p$  is the absolute value of the linear momentum. This complete kinematic measurement produces a data set that can generate angular maps for any fragment or fragment pair provided that the *axial recoil approximation* is valid, i.e., dissociation is sufficiently rapid that the alignment is retained in the measurement. The zenith angle  $\theta$  is defined with respect to  $\vec{\epsilon}$ ,  $\phi$  is the azimuthal angle. The synchrotron (SR) propagation vector is perpendicular to  $\vec{\epsilon}$  and the detector axis. The angular distribution of ions derived by Zare<sup>21</sup> for 100% plane-polarized light is the starting point:

$$I_{\theta,\phi}(\theta, \phi) = \frac{1 + \beta P_2(\cos \theta)}{4\pi}, \quad (9)$$

where  $P_2(x)$  is the second-order Legendre polynomial:  $P_2(x) = (3x^2 - 1)/2$ .  $\beta$  is the anisotropy parameter that characterizes the angular distribution of fragments with respect to the polarisation vector. This parameter can vary from  $-1$  for a purely perpendicular transition to  $+2$  for a purely parallel transition.  $I_{\theta,\phi}(\theta, \phi)$  is normalized so that integration over all solid angle gives 1.

In the case of cylindrical symmetry around  $\vec{\epsilon}$  an integration can be performed over  $\phi$  without loss of information. The normalized distribution over the polar angle then becomes

$$I_{\theta}(\theta) = \frac{\sin \theta [1 + \beta P_2(\cos \theta)]}{2}. \quad (10)$$

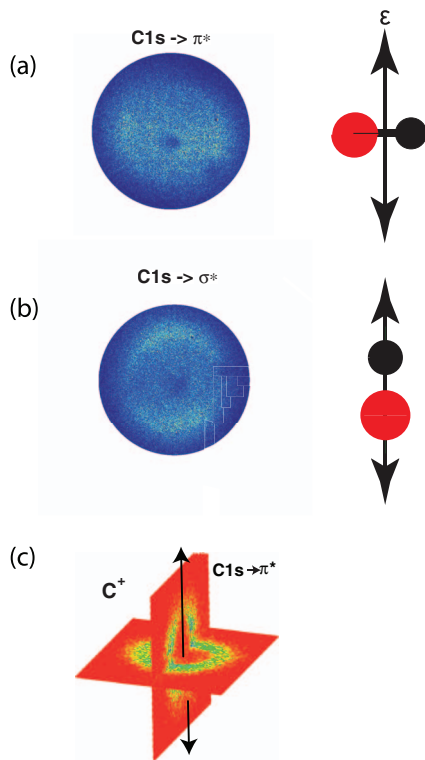


FIG. 6. Time integrated two-dimensional distribution of the  $O^+$  fragment on the detector after excitation to (a)  $C 1s^{-1}\pi^*$  resonance and (b)  $C 1s^{-1}\sigma^*$  resonance. (c) Three-dimensional representation of the  $C^+$  ion momentum at the  $C 1s^{-1}\pi^*$  resonance. The molecular axis is perpendicular to the direction of the polarisation vector,  $\epsilon$ , indicated with a vertical arrow.

Figure 7(b) shows normalized intensity distributions as a function of  $\theta$  for some selected  $\beta$  parameters. For linear molecules such as CO, OCS, and  $C_2H_2$  where the ground state is  $\Sigma$ ,  $\beta = 2$  corresponds to  $\Sigma \rightarrow \Sigma$  transitions, while  $\beta = -1$  corresponds to  $\Sigma \rightarrow \Pi$  transitions.<sup>22</sup> For molecules belonging to other point groups the situation is more complicated.

Since we collect complete fragment angular information, it is possible to extract partial-ion, fragment pair or  $\beta$ -parameters for data subsets. A histogram as a function of  $\theta$  can be plotted in linear momentum space.  $\beta$  is then estimated with a least-squares fit of  $I_\theta(\theta)$  to this histogram and the recoil anisotropy extracted.<sup>23</sup> Figure 7(c) shows the angular distribution of  $C^+$  fragments within the energy interval 11–17.5 eV produced after core-excitation to  $C 1s^{-1}\pi^*$ . The optimal fit for this resonant excitation a function with  $\beta = -0.94$  in good agreement with a  $\Sigma \rightarrow \Pi$  transition within the axial-recoil approximation.

## B. Fragmentation of multiply charged fullerene molecules

A fundamental requirement for time-of-flight mass spectrometry on large molecules and clusters is to resolve nearby masses, e.g., isotopes or protonated molecules. While the separation between masses scales as  $m^{-1/2}$  the peak-width due to thermal energy and extended source volume scales as  $m^{1/2}$ , making it increasingly difficult to resolve large masses. An

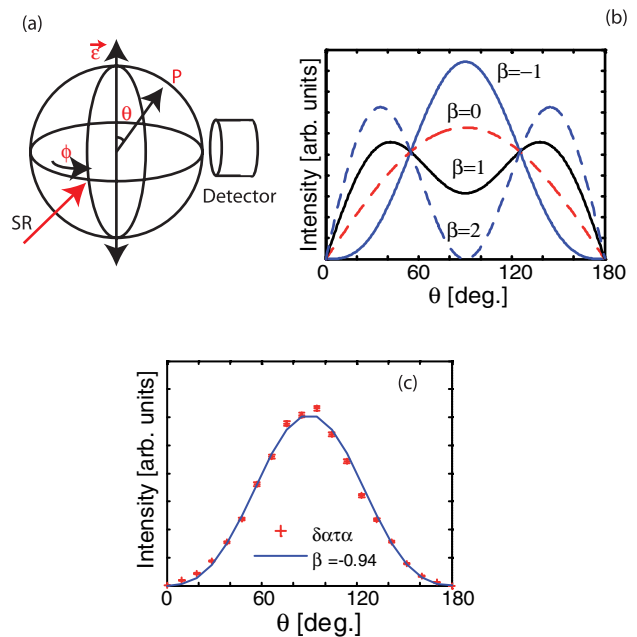


FIG. 7. (a) Schematic diagram of the geometry of the setup.  $\bar{\epsilon}$  is perpendicular to the propagation direction of the synchrotron radiation (SR) and to the spectrometer axis. (b) Calculated angular distributions for different anisotropy parameters obtained from Eq. (10). (c) Measured distribution of  $C^+$  ions as a function of angle  $\theta$  for ions with an energy in the interval 11.0–17.5 eV. Each point represents the integration of  $\phi$  over  $2\pi$ , and over  $\Delta\theta = 10^\circ$ . The solid line shows the best fit of Eq. (10) with  $\beta = -0.94$ .

ideal sample for characterising mass resolution is the  $C_{60}$  fullerene whose lightest isotope has a mass of 720 u.

Figure 8(a) shows a TOF spectrum of the fullerene ions created after core-excitation to the  $C 1s^{-1}\pi^*$  state at 286.2 eV. We observe singly and multiply charged fullerene mother ions,  $C_{60}^{q+}$  with  $q \leq 4$ . To the left of each mother-ion peak a series of fragment peaks are visible  $C_{60-2n}^{q+}$  ( $1 \leq n \leq 7$ ). This is a result of the higher stability of clusters with an even number of carbon atoms and is a well known feature.

In Fig. 8(b) an expanded view of the mother-ion peak region. The peak is split into several mass components due to the presence of two carbon isotopes; the well-resolved peaks clearly demonstrate the excellent mass resolution up to 725 u. The intensity distribution of the peaks can be described by a discrete binomial probability function,  $B_j^n(k)$ , where  $n = 60$  is the number of atoms,  $j = 0.011$  is the natural abundance of  $^{13}C$ , and  $k \in \{0, 1, 2, \dots, 5\}$  is the number of  $^{13}C$  atoms in the fullerene. The combined peak profile for the mother ion  $C_{60}^{q+}$ , assuming thermal beam energies is

$$P_1(T; q) = \sum_k B_j^{60}(k) \cdot F_{T_0(k, q)}^{\text{therm}}(T), \quad (11)$$

where  $F_{T_0(k, q)}^{\text{therm}}(T)$  gives a Gaussian peak centered on the nominal time of flight  $T_0(k, q)$  for  $m = (720 + k)$  u.

A least-squares fit provides a value for the thermal broadening along the spectrometer axis allowing extraction of the  $p_z$  distribution. The analysis is carried out in the temporal domain in order to be able to account for delayed fragmentation. We find a mean thermal broadening of  $3.5 \pm 1.5$  meV with a monotonic increase from the singly charged to quadruply charged fullerenes. This extremely low temperature reflects



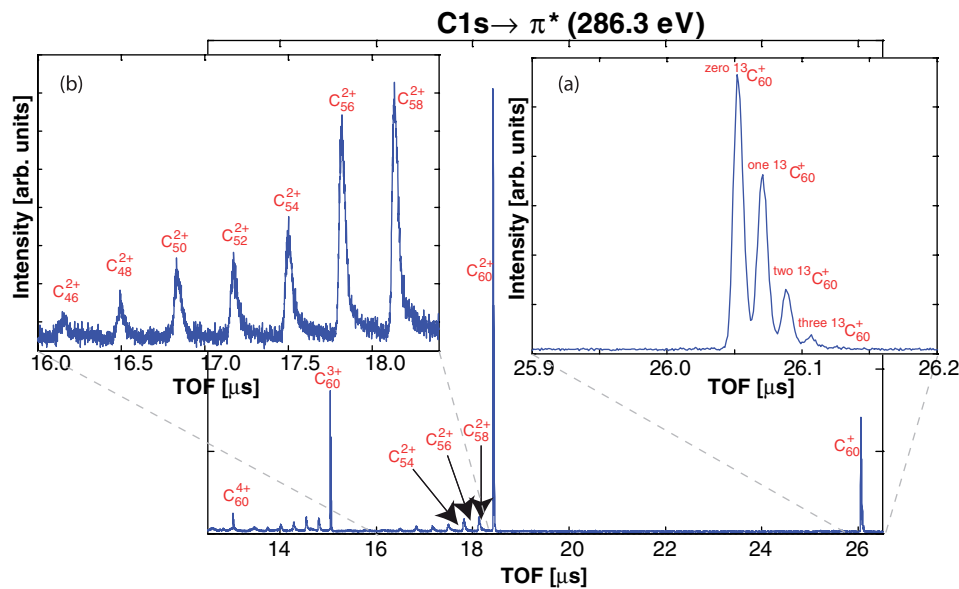


FIG. 8. TOF spectrum after core-electron excitation to the C  $1s^{-1}\pi^*$  state at 286.2 eV. The subplots show (a) the mass spectrum of the isotopes of fullerene and (b) of the doubly charged fullerene and its fragments.

the cooling of the molecular beam in its transverse direction (the  $z$  direction of the spectrometer). This reduced velocity along the spectrometer axis is optimal for accurate ion recoil determination. The momentum distribution along the beam is between one and two orders of magnitude larger due to the distribution of velocities in the fullerene beam as discussed by Katayanagi and Mitsuke.<sup>24</sup>

Figure 8 shows the primary dissociation channels of the dication  $C_{60-2n}^{2+}$  for  $1 \leq n \leq 7$ . The isotope structure is smeared out for higher charge states due to the kinetic energy imparted to fragments upon dissociation. The peak shapes of these species have a pronounced asymmetry toward longer flight time, and the central flight times are shifted by up to 10 ns. The shift cannot be related to an error in the mass calibration, since flight times of the singly and multiply charged mother ions are predicted by Eq. (2) within 500 ps. Assuming that thermal velocities in the source are responsible is also not sufficient to reproduce the peak shapes.

Fragmentation of  $C_{60}$  molecules was investigated after ionization with 200 eV electrons by Foltin *et al.*<sup>25</sup> They showed that the production of  $C_{56}^{2+}$  and  $C_{56}^{3+}$  preferentially occurs by stepwise ejection of neutral carbon dimers. Such a stepwise process could both create a delay in the ion flight time and affect the kinetic energy. Based on this we model the peak shape with a distribution based on the convolution of a Gaussian and an exponential decay,

$$D_{T_0, E_k, \tau}(T) = [F_{T_0}^{E_k} * F_{\tau}](T), \quad (12)$$

where  $F_{T_0}^{E_k}(T)$  is a Gaussian distribution to model an isotropic fragmentation process with an average fragment kinetic energy of  $E_k$ .  $F_{\tau}(t) \propto e^{-t/\tau}$ ,  $t > 0$  represents the decay of a highly excited metastable state with lifetime  $\tau$ . In the limit  $\tau \rightarrow 0$  the exponential decay becomes a  $\delta$ -function and  $D$  becomes  $F_{T_0}^{E_k}$ . To both reproduce the apparent shift of the central time and accurately fit the “tail” towards longer flight times, two decay processes with different lifetimes were required. The resulting

distribution for  $C_{60-2n}^{q+}$  is given by

$$P_2(T; q, n, E_k) = \sum_k B_j^{60-2n}(k) [I_{\tau_1} \cdot D_{T_0(k, q), E_k, \tau_1}(T) + I_{\tau_2} \cdot D_{T_0(k, q), E_k, \tau_2}(T)]. \quad (13)$$

This model reproduces the mass spectra for  $n \leq 4$  and  $q \in \{2, 3\}$  remarkably well. The lifetimes of the decay mechanisms are  $\tau_1 = 14 \pm 2$  ns and  $\tau_2 = 150 \pm 13$  ns with a branching ratio  $I_{\tau_2}/I_{\tau_1} = 0.4 \pm 0.1$ . The kinetic energy of the fragmented fullerene in the laboratory frame increases from 200 meV to 1 eV as  $n$  increases. The charge does not seem to be an important parameter. In order for the fitting procedure to converge properly, we restricted the data to ions near the center of the detector ( $R \leq 8$  mm). Evidence that a weak contribution of low mass fragments,  $C_{4k+3}^+$  ( $2 \leq k \leq 4$ ), with relatively high kinetic energy affects the mass spectra was also found. Finally, we note that the peak profile of high mass fragments  $C_{60-2n}^{q+}$  with  $n \geq 5$  becomes almost symmetric, probably because they are emitted together with small  $C_x$  units ( $3 \leq x \leq 9$ ). This suggests that more complex fragmentation mechanisms than sequential emission of neutral  $C_2$  are required to produce these fragments. The detailed investigation of the fragmentation mechanisms will be the subject of a future publication.

#### IV. CONCLUSION

The design of an imaging spectrometer for three-dimensional ion momenta and the theoretical basis for the implementation of a focusing lens for ions from an extended source volume are described. The spectrometer is shown both by simulation and by selected samples to fulfil these criteria for kinetic energies typical for photo-induced dissociation of molecules. We discuss the transformation of data to linear momentum coordinates using a semi-analytical

approach. The measurement of multi-ion momentum and angle is demonstrated for dissociation of the carbon monoxide dication. The spectrometer is capable of high resolution even for large masses, thus making it suitable for cluster measurements. The mass spectra of fullerene ions demonstrates the high performance by resolving isotopes of the non-dissociated mother ion and investigating the dynamics of dissociation of a multiply charged fullerene. This opens up the possibility to use deuterium marking in photochemical reactions as is commonly done for biological macromolecules.

- <sup>1</sup>I. Nenner, and P. Morin, in *VUV and Soft X-ray Photoionization*, edited by U. Becker and D. A. Shirley (Springer Verlag, Berlin, 1996).
- <sup>2</sup>R. Dörner, V. Mergel, O. Jagutzki, L. Spielberger, J. Ullrich, R. Moshammer, and H. Schmidt-Böcking, *Phys. Rep.* **330**, 95 (2000).
- <sup>3</sup>R. Continetti, *Annu. Rev. Phys. Chem.* **52**, 165 (2001).
- <sup>4</sup>K. Ueda and J. H. D. Eland, *J. Phys. B* **38**, S839 (2005).
- <sup>5</sup>I. V. Hertel and W. Radloff, *Rep. Prog. Phys.* **69**, 1897 (2006).
- <sup>6</sup>M. Takahashi, J. Cave, and J. H. D. Eland, *Rev. Sci. Instrum.* **71**, 1337 (2000).
- <sup>7</sup>M. Lebech, J. C. Houver, and D. Dowek, *Rev. Sci. Instrum.* **73**, 1866 (2002).
- <sup>8</sup>G. A. Garcia, L. Nahon, C. J. Harding, E. A. Mikhajlo, and I. Powis, *Rev. Sci. Instrum.* **76**, 053302 (2005).

- <sup>9</sup>G. Prümper, H. Fukuzawa, T. Lischke, and K. Ueda, *Rev. Sci. Instrum.* **78**, 083104 (2007).
- <sup>10</sup>C. Miron, P. Morin, D. Céolin, L. Journel, and M. Simon, *J. Chem. Phys.* **128**, 154314 (2008).
- <sup>11</sup>D. Holland and D. Shaw, *Chem. Phys.* **409**, 11 (2012).
- <sup>12</sup>D. Chandler and P. Houston, *J. Chem. Phys.* **87**, 1445 (1987).
- <sup>13</sup>J. H. D. Eland and A. Pearson, *Meas. Sci. Technol.* **1**, 36 (1990).
- <sup>14</sup>A. T. J. B. Eppink and D. H. Parker, *Rev. Sci. Instrum.* **68**, 3477 (1997).
- <sup>15</sup>A. I. Chichinin, T. Einfeld, C. Maul, and K.-H. Gericke, *Rev. Sci. Instrum.* **73**, 1856 (2002).
- <sup>16</sup>W. Wiley and I. McLaren, *Rev. Sci. Instrum.* **26**, 1150 (1955).
- <sup>17</sup>D. A. Dahl, *Int. J. Mass Spectrometry* **200**, 3 (2000).
- <sup>18</sup>D. P. Seccombe and T. J. Reddish, *Rev. Sci. Instrum.* **72**, 1330 (2001).
- <sup>19</sup>N. Saito, F. Heiser, O. Hemmers, K. Wieliczek, J. Viehhaus, and U. Becker, *Phys. Rev. A* **54**, 2004 (1996).
- <sup>20</sup>L. Journel, R. Guillemin, A. Haouas, P. Lablanquie, F. Penent, J. Palaudoux, L. Andric, M. Simon, D. Céolin, T. Kaneyasu, J. Viehhaus, M. Braune, W. B. Li, C. Elkharrat, F. Catoire, J.-C. Houver, and D. Dowek, *Phys. Rev. A* **77**, 042710 (2008).
- <sup>21</sup>R. N. Zare, *Mol. Photochem.* **4**, 1 (1972).
- <sup>22</sup>J. Stöhr, *NEXAFS Spectroscopy* (Springer Verlag, 1992), pp. 48–75.
- <sup>23</sup>Z. Pestic, D. Rolles, M. Perri, R. Bilodeau, G. Ackerman, B. Rude, A. Kilcoyne, J. D. Bozek, and N. Berrah, *J. Electr. Spectr. Rel. Phenom.* **155**, 155 (2007).
- <sup>24</sup>H. Katayanagi and K. Mitsuke, *J. Chem. Phys.* **133**, 081101 (2010).
- <sup>25</sup>M. Foltin, O. Echt, P. Scheier, B. Dünser, R. Wörgötter, D. Muigg, S. Matt, and T. D. Märk, *J. Chem. Phys.* **107**, 6246 (1997).